Available online at www.sciencedirect.com
SCIENCE DIRECT®
International Journal of Heat and Mass Transfer 48 (2005) 2023–2031
International Journal of HEAT and MASS TRANSFER
www.elsevier.com/locate/ijhmt

Thermal property measurement of thin aluminum oxide layers for giant magnetoresistive (GMR) head applications

Bahareh Behkam, Yizhang Yang, Mehdi Asheghi *

Department of Mechanical Engineering, Data Storage Systems Center (DSSC), Carnegie Mellon University, Pittsburgh, PA 15213-3890, USA

Received 30 January 2004; received in revised form 23 July 2004
Available online 4 March 2005

Abstract

In recent years, the magnetic recording storage industry has developed a growing interest in increasing recording density of the magnetic disks. Since dimensions of the recording head read transducer have been scaled down to increase areal density, all other parameters being equal, the energy required to cause damage by an ElectroStatic Discharge (ESD) event is reduced substantially. The present work characterizes the thermal transport properties of Al_2O_3 gap layer, which are essential to address the ESD failure. This study provides data for out-of-plane thermal conductivity of thin Al_2O_3 layers, which are obtained using steady-state Joule heating and electrical-resistance thermometry technique.

Keywords: Aluminum oxide; Boundary resistance; GMR; Self-heating

1. Introduction

Magnetic recording systems, which utilize magnetic disks and tape drives, constitute the main form of data storage and retrieval in present-day computer and data processing systems. The stored information is retrieved, in the reading process, by scanning a reading head over the recording medium. The widely used GMR head, works based on the magnetoresistance phenomenon, which is the change in resistance of a conductor when a magnetic field is applied to it. The reading head intercepts the magnetic flux from magnetization patterns on the recording medium and converts it into a resistance change signal, which is then detected and decoded. A typical three-dimensional geometry of the GMR head is shown in Fig. 1. The GMR element is embedded within thin dielectric aluminum oxide gap layers. The relevant dimensions of the GMR heads are listed in Table 1 for data storage recording densities of 2.8–80 Gbits in^{-2}. It can be seen that with increase in recording density, the thickness of the gap layer decreases substantially such that by year 2005 the Al_2O_3 layers thickness of less than 26 nm is expected.

Since the gap dielectric layer has much lower thermal conductivity than the metallic GMR layer, the heat generated during an ESD event is forced in the lateral direction toward the large area lead contacts. The shape of the temperature distribution in the GMR layer and the extent of lateral diffusion into the GMR and/or lead layers depends on the thermal conductivities and

* Corresponding author. Tel.: +1 412 268 2509.
E-mail address: masheghi@andrew.cmu.edu (M. Asheghi).

0017-9310/$ - see front matter © 2005 Elsevier Ltd. All rights reserved.
doi:10.1016/j.ijheatmasstransfer.2004.12.010

Nomenclature

A_c	cross-sectional area of the fin (m^2)
$A_{effective}$	effective area of the conduction from the GMR element to the substrate (m^2)
d	thickness of the layer (m)
h_{GMR}	height of the GMR element (m)
h	convective heat transfer coefficient ($W\,m^{-2}\,K^{-1}$)
I	electrical current (A)
k	thermal conductivity ($W\,m^{-1}\,K^{-1}$)
k_{base}	nominal value of thermal conductivity used in simulations ($W\,m^{-1}\,K^{-1}$)
$k_{n,eff}$	effective normal thermal conductivity of the gap layer ($W\,m^{-1}\,K^{-1}$)
L	length of the heater bridge (m)
L_h	thermal healing length for the lead layer (m)
m	$\sqrt{\frac{hP}{kA_c}}$, defined in Eq. (A.3) (m^{-1})
P	fin perimeter (m)
Q	heat dissipated in bridge A (W)
$\dot{q}$	heat generation within the fin ($W\,m^{-3}$)
R	electrical resistance (Ω)
R_{1D}	one-dimensional thermal resistance of the gap layer ($K\,W^{-1}\,m^2$)
R_{2D}	two-dimensional thermal resistance of the gap layer ($K\,W^{-1}\,m^2$)
R_B	thermal boundary resistance ($K\,W^{-1}\,m^2$)
R_T	total thermal resistance of the gap layer ($K\,W^{-1}\,m^2$)
$R_{th,\,GMR}$	normal thermal resistance of the GMR head ($K\,W^{-1}$)
T	temperature (K)
T_b	temperature at the base of the fin (K)
T_{base}	temperature of the GMR element, computed for $k_{Gap} = k_{base}$ (K)
T_∞	temperature of the environment (K)
U	uncertainty function, defined in Eq. (8)
V	voltage (V)
w	width of the GMR element (m)
W	width of the test structure (m)
X_{CC}	center to center separation distance between the heater and thermometer bridges (m)

Greek symbols

α	temperature coefficient of electrical resistance (K^{-1})
ΔT	change in temperature (K)
λ_i	eigenvalues, used in Eq. (6) (m^{-1})
θ	Incident angle (°)
Θ	excess temperature, $T(x) - T_\infty$ (K)
Θ_b	excess temperature at the base of the fin, $T_b - T_\infty$ (K)
ψ	ratio of one-dimensional thermal resistance to the two-dimensional thermal resistance of the gap layer, defined in Eq. (6)

Subscripts

A	refers to properties of bridge A
B	refers to properties of point B
C	refers to properties of bridge C
Gap	refers to properties of the gap layer
GMR	refers to properties of the GMR element
Lead	refers to properties of the lead layer

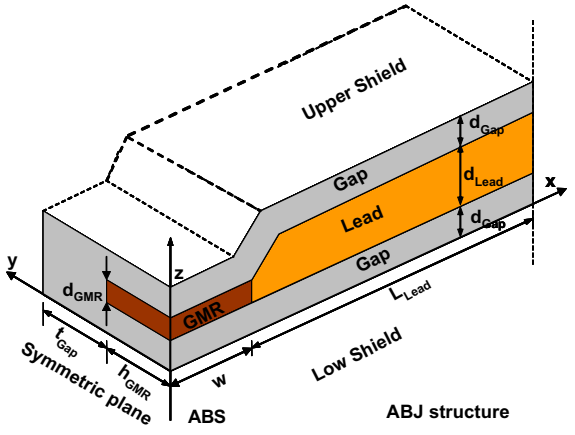

Fig. 1. Three-dimensional schematic of the GMR head.

corresponding thicknesses of the GMR, lead and gap layers. A simplified analysis of the ESD event suggests that in quasi-steady state condition, assuming the same thermal conductivity and thickness for the GMR and lead layers, the thermal healing length for the lead layer, which is a measure of the extent of the lateral diffusion in the lead interconnect, can be defined by (see Appendix A)

$$L_h \approx (d_{Gap} d_{GMR} k_{GMR}/k_{Gap})^{1/2} \tag{1}$$

where k_{GMR} is the GMR/lead thermal conductivity, k_{Gap} is the gap thermal conductivity and d_{GMR} and d_{Gap} are the GMR (or lead) and gap layer thickness, respectively. The steady-state normal thermal resistance of the GMR head can be approximated by

$$R_{th,GMR} \approx \frac{d_{Gap}}{k_{Gap} 2A_{effective}} \tag{2}$$

According to the above equation, the thermal resistance of the GMR head is mainly due to the heat loss from the top and bottom gap layers. The effective area for conduction to the substrate can be defined as

Table 1
GMR dimensions vs. recording density/year [1]

Year	Recording density (Gbits in^{-2})	Width, w (μm)	Height, h_{GMR} (μm)	GMR thickness, d_{GMR} (nm)	Gap thickness, d_{Gap} (nm)
1997	2.8	1.2	1	50	70
1998	5	1.05	0.7	44	61
2000	10	0.72	0.5	36	50
2001	20	0.5	0.3	28	39
2002	40	0.3	0.18	21	31
2003	80	0.205	0.11	18	26

$$A_{\text{effective}} \approx (2L_h + 2w) \times h_{GMR} \quad (3)$$

where h and w are the height and width of the GMR head, respectively, as shown in Fig. 1. Therefore, the normal thermal resistance of the GMR head scales with thermal conductivity of the alumina gap layer such that

$$R_{th,GMR} \propto (k_{Gap})^{-1/2} \quad (4)$$

As a result, the thermal conductivity of the gap layer, which is a strong function of the fabrication process, is crucial for an accurate prediction of self-heating, ESD threshold voltage in the GMR head. Yang et al. [2] performed extensive self-heating and ESD failure simulations in GMR heads and have shown that the thermal conductivity of the gap layer can largely influence the temperature rise in the GMR sensor. Fig. 2 shows the normalized steady-state temperature rise change with the thermal conductivity of the gap layer, varied from nominal values for different magnetic recording areal density. The thermal conductivity of gap layer has a strong effect on the temperature rise in GMR sensor. For instance, for 20 Gbits in^{-2} areal density, 30% reduction in k_{Gap} will result in nearly 18% increase in the temperature of the GMR element, which is consistent with Eq. (4). The effect of k_{Gap} becomes smaller for the GMR head beyond areal density of 20 Gbits in^{-2}, due to variations in geometry and dimensions of the read head constituent elements.

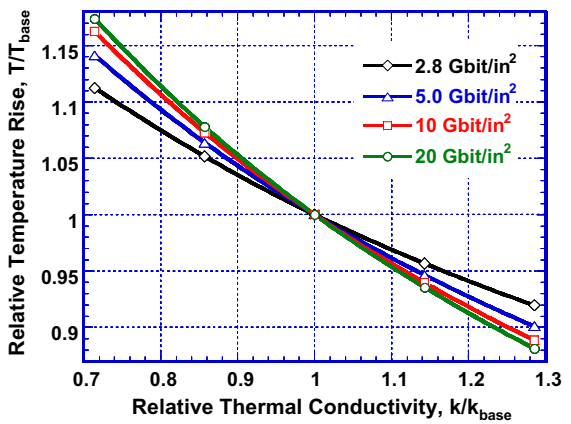

Fig. 2. Sensitivity of the GMR temperature rise to the variation in gap layer thermal conductivity, k_{Gap}, at different areal density, where the k_{base} = 1 W m^{-1} K^{-1}.

Aluminum oxide is one the most popular dielectrics which have been used in data storage industry for quite a long time. The interest in aluminum oxide films stems from the following experimental observations: (1) the ionic mobility of impurities (Na^+) is very low in these films, (2) their dielectric constant is double that of silicon oxide [3]. However, relatively little has been reported on the deposition of aluminum oxide by RF sputtering on silicon or other substrates. Sputtering usually yields films with good compositional uniformity throughout the thickness of the film as opposed to other methods such as evaporation method [4]. Nevertheless analytical evidence has been presented which shows that sputtered alumina is oxygen deficient compared to stoichiometric $A1_2O_3$, and also contains argon from the sputtering process [5]. The sputtered alumina films have been examined by numerous investigators and found to be amorphous [3–6]. Characteristics of the alumina films such as etch rate, density, refractive index, dielectric constant, conductivity and young modulus are dependent upon deposition parameters, e.g., base pressure, sputtering pressure, power density and substrate bias. Pervious works were aimed on the effect of sputtering power density on the alumina film physical and electrical properties [3] and also the effect of pressure of the sputtering atmosphere on the film physical properties [6]. There is also some work done on composition and stability of the RF sputtered alumina films [5]. While significant research efforts have been on the material characterization of thin aluminum oxide layer, thermal characterization of these materials has received very little attention. Table 2 shows some of the thermal conductivity values that are

Table 2
Thermal conductivity of Al_2O_3

k (W m^{-1} K^{-1})	References
1	Ju et al. [7]
3.5	Chang [8], Young [9]
~16	Wallash [10], Greason [11]
~25	Bulk ceramic [12]

commonly used in the literature. The only experimental value is reported by Ju et al. [7]. They used 3ω thermometry technique and found the effective thermal conductivity for 30–50 nm of the alumina gap layer to be approximately 1.0 $W\,m^{-1}\,K^{-1}$. No information regarding the gap layer deposition method and dependency of the thermal conductivity values upon thickness is reported. It is well established that the thermal transport properties of microfabricated thin dielectric [13] and passivation [14] layers are substantially lower than the bulk material. The reduction in thermal conductivity can be a result of thin film microfabrication process, which significantly influences the material microstructure. Therefore, it is critical to follow the same fabrication process in the deposition of the test samples.

In this work, normal thermal conductivity of 10, 20, 40, 60, 80 and 100 nm layers of alumina are measured using steady-state Joule heating and thermometry technique. Material characteristics of the alumina film in each of these test structures have been inspected using two different X-ray diffraction (XRD) methods and finally thermal conductivity of alumina films at room temperature has been measured. Each measurement is complemented with corresponding uncertainty analysis.

2. Fabrication and characterization of the experimental structure

Alumina was RF sputtered on silicon wafer using Perkin–Elmer 8L sputtering machine. The alumina target used was a sintered aluminum oxide (99.995%) disk 4 in. in diameter and 1 cm thick. It was metallized on one side and bonded using silver epoxy to flat water-cooled aluminum disk. Ultra high-purity argon (99.999%) was used as the sputtering gas and the pressure during sputtering was kept constant by controlling argon flow rate. In a typical run, base pressure of the system was 2×10^{-7} Torr. Temperature of the substrate was measured using series 21 tempilable and it is known to be more than 260 °C. Using the same sputtering machine a 500 nm layer of Al/Cu was sputtered on top of alumina layer. Samples were then patterned using GCA 4800 wafer stepper photolithography system. Aluminum bridges were etched out in commonwealth scientific ion beam etching system. In the last step the photoresist on top of metal bridges was removed in IPC barrel etcher.

Deposited alumina films were inspected using conventional XRD and also glancing incidence scan methods. X-ray generator Philips X'Pert was used for both of scans. From glancing incidence results, Fig. 3, films appears to be amorphous alumina. However, conventional XRD results illustrated in Fig. 4 indicate that some crystalline grains of aluminum also exist in the samples. Percentage of the aluminum seems to be insignificant because the film is electrically insulator and it is translucent like alumina. In depth investigation of the film composition is beyond the context of this paper and can be found by Rutherford backscattering spectrometry analysis.

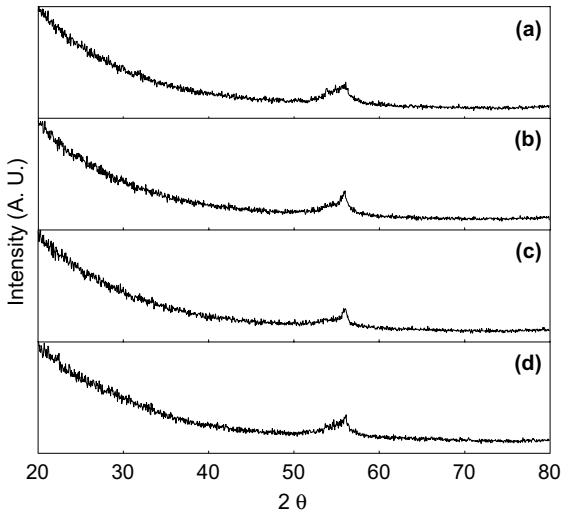

Fig. 3. Glancing incidence scan of the deposited alumina films for (a) 10 nm, (b) 20 nm, (c) 40 nm and (d) 80 nm samples.

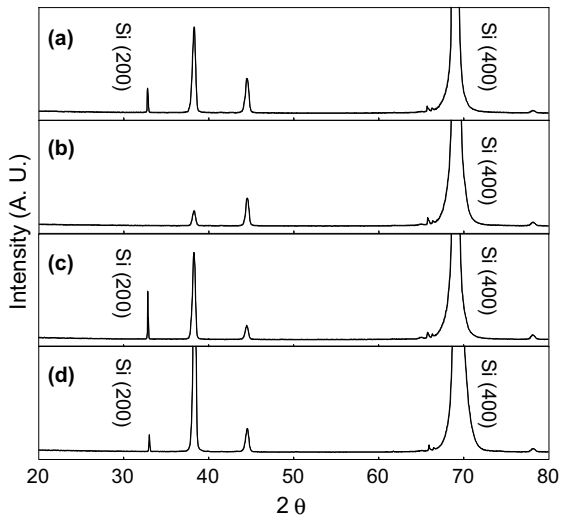

Fig. 4. Conventional XRD scan of the alumina sample for (a) 10 nm, (b) 20 nm, (c) 40 nm and (d) 80 nm samples.

3. Experimental technique

Thermal conductivity of the gap layer is measured using electrical-resistance thermometry technique [15]. Fig. 5 depicts schematic of the test structure used to

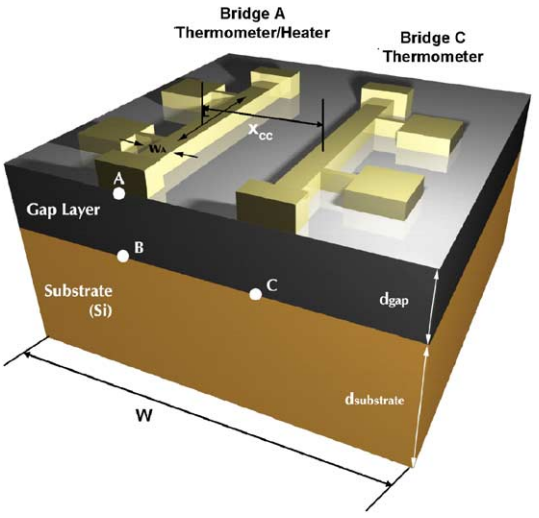

Fig. 5. Schematic of the test structure. The left aluminum bridge is used both as the heater and thermometer where its width and length are given by w_A and L, respectively (see Table 3). The right bridge is used only as a thermometer.

measure gap layer out-of-plane (normal) thermal conductivity. Two parallel aluminum bridges are patterned on the sample layer. Bridge A carries a large current density, serving as both heater and thermometer, while bridge C carries a low current density and serves only as a thermometer. The microfabricated test structure was wire bonded in a 68 pin LCCs chip carrier to provide electrical access to the bridges (Fig. 6). The power, Q, dissipated in bridge A is conducted through the gap layer and silicon substrate, resulting in a temperature gradient across the layer. The temperatures of point A, T_A, and point C, T_C, are determined from the change in electrical resistances of the bridges A and C. The

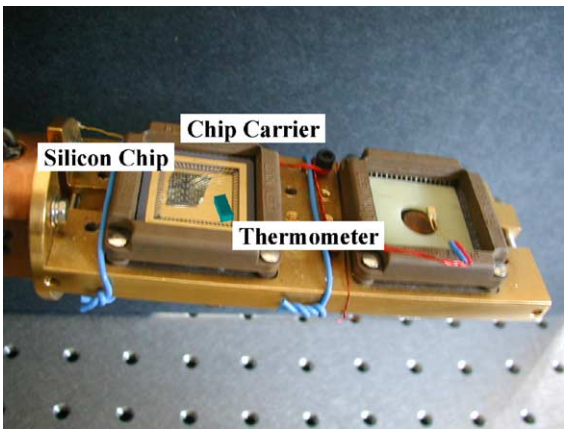

Fig. 6. Image of the test structure placed in the chip carrier and wire bonded.

electrical resistances of the thermometer bridges were measured using the four-point (wire) resistance measurement technique, to eliminate the contribution of the electrical contact resistances. In order to calibrate the temperature dependency of the electrical resistance of the bridges, the test structure was heated using the Cryostat's heater which is placed in the vicinity of the chip carrier. During the calibration process the current in the metal bridges are kept at minimum possible to avoid self-heating. A thermometer with the accuracy of ±50 mK is placed on the chip carrier next to the test structure, shown in Fig. 6. The temperature of the chip carrier was controlled using a model 331S temperature controller. For different settings of the temperature, resistance of the bridges and sensor's temperature were recorded.

The width of the bridge A, is chosen to be much larger than the thickness of the gap layer, so that the heat conduction is nearly one-dimensional normal to the gap layer. Bridge C is located at a proper distance from bridge A, such that there is no temperature gradient across the gap layer. Therefore, changes in the resistance of the bridge C, represents changes in the temperature of the point C, in the substrate. As shown in Fig. 5, point B is inaccessible for thermometry; therefore temperature of the point T_B is calculated using the measured value of T_C by solving the two-dimensional heat conduction in the substrate [15]. In this approach the thermal boundary resistance at the interface of the chip and the chip-carrier is eliminated during the steady-state measurements. The effective normal conductivity of the gap layer, $k_{n,\mathrm{eff}}$, can be calculated from

$$k_{n,\mathrm{eff}} = \frac{d_{\mathrm{Gap}}}{\psi}\frac{Q/(w_A L)}{T_A - T_B} \tag{5}$$

where w_A and L are width and length of the heater bridge, respectively. The parameter ψ is the ratio of the one-dimensional thermal resistance, $R_{1D} = d_{\mathrm{Gap}}/k_{\mathrm{Gap}}$, over the two-dimensional thermal resistance of the gap layer. Its value depends on the ratio of w_A/d_{Gap} and account for the two-dimensional conduction in the gap layer. The R_{2D} is obtained by solving the two-dimensional heat conduction in the gap layer with a uniform heat flux boundary condition at top surface for the width of w_A, and adiabatic boundary condition for the rest of the length of the top surface, isothermal condition at bottom surface and on the right hand side, and adiabatic boundary condition on the left hand side. The solution yields an equivalent thermal resistance R_{2D} which is the ratio of average temperature rise of width w_A at top surface, over the heat flux applied to the gap layer. ψ can be approximated by [15]

$$\psi = \frac{W w_A d_{\mathrm{Gap}}}{4\sum_{i=0}^{\infty}\tanh(\lambda_i d_{\mathrm{Gap}})\sin^2(\lambda_i w_A/2)/(\lambda_i^3)} \tag{6}$$

where W is the width of the test structure and the eigenvalues are given by $\lambda_i = \frac{\pi}{W}\left(\frac{2i+1}{2}\right)$.

4. Experiments and results

Experiment was performed for six samples with different thicknesses for alumina film. As it is demonstrated in Fig. 5, thermometer bridge C is to measure the temperature of point C, which is at the interface of the alumina layer and silicon substrate. Therefore, it is absolutely crucial to have the appropriate separation between heater and thermometer bridges such that the thermometer only senses the temperature rise at point C which is resulted from substrate temperature rise. At the same time, if bridge C is located too far from bridge A, the temperature rise at point C will be negligible and not nearly enough to infer the temperature at the location B. In order to determine the optimized separation distance between bridge A and C, two-dimensional heat conduction analysis for the gap/silicon substrate bi-layer was performed. As shown in Table 3 for a given gap layer thickness and thermal conductivity there will be an optimum separation distance between the bridges A and C (X_{CC} (min)). However, the separation distance between the bridges in the photolithography mask was designed to be generic since the gap thermal conductivity and thickness are unknown prior to the measurements. Table 3 shows dimensions of the bridges, separation distance between the bridges for sample and also the optimum separation distance estimated from the analytical solution described in the above.

The extracted temperature differences between points A and B from the experiments and predictions based on Eq. (5) are plotted as function of the heating current in Fig. 7, using the $k_{n,\text{eff}}$ (or k_{Gap}) as a fitting parameter. This analysis was repeated for different gap layer thickness and the effective thermal resistance of the gap layer, R_T, was obtained by taking the ratio of $d_{\text{Gap}}/k_{\text{Gap}}$. The experimental results for thermal resistance of the alumina layer as a function of thickness are illustrated in Fig. 8. Thermal resistance of this film includes the resistance of the film itself along with the Al/Al_2O_3/Si boundary resistances. Experimental data can be extrapolated to zero gap layer thickness to obtain the thermal boundary resistance, R_B. For gap layers of thickness less than 60 nm, the contribution of the boundary resistance to the total amount of resistance is significant. This has serious implications for the data storage industry as further reduction in thickness of the gap layer in an attempt to reduce the self-heating of these devices is not going to be a viable approach.

Table 3
Dimensions of the test structures

Gap layer thickness (nm)	Heater width (μm)	Thermometer width (μm)	X_{CC} separation (μm)[a]	X_{CC} (min) separation (μm)[b]
10	22	2	12	3
20	2	2	7	4
40	10	2	11	7.5
60	10	2	16	8
80	2	2	12	9.5
100	2	2	12	10

[a] Center to center separation distance between heater and thermometer.
[b] Minimum required center to center separation.

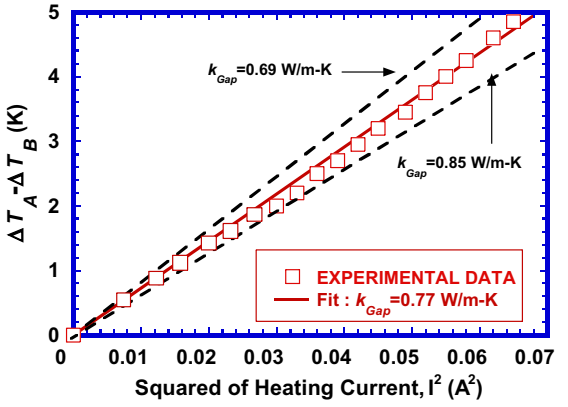

Fig. 7. Temperature gradient across the gap layer for different level of heating currents.

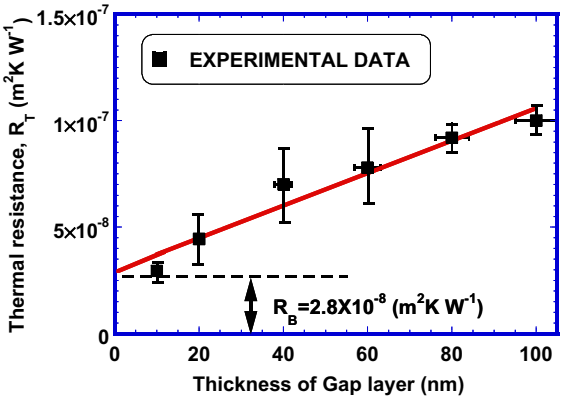

Fig. 8. Experimental data for the thermal resistance of Al_2O_3 gap layers as a function of layer thickness. The intercept of the linear fit curve with the y axis yields thermal boundary resistance of 2.8×10^{-8} m^2 K W^{-1}.

5. Uncertainty analysis

Uncertainty in the presented data is due to (1) uncertainty in indirect measurement of temperature at point

B, (2) uncertainty in thickness of the sample layer and dimensions of the bridges, (3) uncertainty in temperature coefficient of electrical resistance, (4) uncertainty of the measurement devices. The total thermal resistance across the gap layer is related to the measured quantities by [15]

$$R_T = \frac{[\Delta T_A]_{\text{experiment}} - [\Delta T_C]_{\text{experiment}} - [\Delta T_B - \Delta T_C]_{\text{analysis}}}{Q/(wL)} = \frac{\Delta\left(\frac{V_A}{I_A}\right)\left(\frac{dR_A}{dT_A}\right)^{-1} - \Delta R_C\left(\frac{dR_C}{dT_C}\right)^{-1} - [\Delta T_B - \Delta T_C]_{\text{analysis}}}{I_A V_A/(wL)} \quad (7)$$

where V_A and I_A are the voltage drop and current measured from bridge A and R_C is the resistance measured from bridge C. $\Delta(V_A/I_A)$ and ΔR_C are the changes in resistances of bridges A and C when I_A is increased. The uncertainty in the bridge length L is negligible. For simplicity $\Delta(V_A/I_A)$ and ΔV_A are treated independently. The total uncertainty in the thermal resistance is calculated from the following equation [15]:

$$\begin{aligned}[U(R_T)]^2 = {} & \left[U\left(\frac{dR_A}{dT_A}\right)\right]^2\left[\frac{\Delta T_A}{\Delta T_A - \Delta T_B}\right]^2 + \left[U\left(\Delta\left(\frac{V_A}{T_A}\right)\right)\right]^2\left[\frac{\Delta T_A}{\Delta T_A - \Delta T_B}\right]^2 + \left[U\left(\frac{dR_C}{dT_C}\right)\right]^2\left[\frac{\Delta T_C}{\Delta T_A - \Delta T_B}\right]^2 \\ & + [U(\Delta V_C)]^2\left[\frac{\Delta T_C}{\Delta T_A - \Delta T_B}\right]^2 + [U[\Delta T_B - \Delta T_C]_{\text{analysis}}]^2\left[\frac{\Delta T_B - \Delta T_C}{\Delta T_A - \Delta T_B}\right]^2 \\ & + [U(V_A)]^2 + [U(I_A)]^2 + [U(w_A)] \end{aligned} \quad (8)$$

The value of uncertainty for $[\Delta T_B - \Delta T_C]_{\text{analysis}}$ is unknown. A special structure with two thermometer bridges is required for measuring this parameter. Measurement is currently under progress; however, from previous work [15] this value is speculated to be less than 10%. Assuming a value of 10% for $[\Delta T_B - \Delta T_C]_{\text{analysis}}$, Eq. (8) yields an uncertainty of 15.2%, 10.9%, 27.6%, 24.9%, 7.0% and 6.3% for 10, 20, 40, 60, 80 and 100 nm samples, respectively. Uncertainty of $[\Delta T_B - \Delta T_C]_{\text{analysis}}$ was then reduced to 5% however the total uncertainty for all samples changed to 14.5%, 10.7%, 26.8%, 24.4%, 6.7% and 6.2% for 10, 20, 40, 60, 80 and 100 nm samples.

Thickness of the alumina film was measured using a KLA Tencor surface profiler over a 3-in. wafer and a variation of maximum 5% was observed. The widths of heater bridges of the test structures were measured using Scanning Electron Microscopy (SEM). The temperature coefficient of the electrical resistance, α, was measured to be around $3 \times 10^3\ \text{K}^{-1}$ at 300 K with the estimated error of ±2%, which is due to the fact that the temperature sensor was slightly further away from the LCC chip carrier.

6. Summary and conclusions

The normal thermal conductivity of 10, 20, 40, 60, 80 and 100 nm sputtered alumina film was measured using steady-state Joule heating and electrical-resistance thermometry. The experimental data were used to obtain thermal boundary resistance at the interface, which is in near $2.8 \times 10^{-8}\ \text{m}^2\ \text{K W}^{-1}$. It was concluded that the contribution of the boundary resistance to the total thermal resistance is quite significant for gap layers of thickness less than 60 nm. The thermal conductivity of 100 nm gap layer is estimated from the measurements to be $\sim$1 W m^{-1} K^{-1}. If this value is used as the nominal thermal conductivity of the 10 nm gap layer instead of the measured value of $k_{\text{Gap}} = 0.33\ \text{W m}^{-1}\ \text{K}^{-1}$, the value of thermal conductivity will be overestimated by 67%. As a result, according to Eq. (4), which is also consistent with the simulations results shown in Fig. 2, the thermal resistance of GMR sensor could be underestimated by nearly 75% using the inappropriate value for thermal conductivity of the ultra-thin gap layers.

This has serious implications for the data storage industry as further reduction in thickness of the gap layer in an attempt to reduce the self-heating of these devices will not be a viable approach. Perhaps the only way to reduce the thermal boundary resistance would be to improve the quality of the interfaces.

Acknowledgements

Authors would also like to acknowledge the support from data storage systems center(DSSC). This work is partially supported by a grant from National Science Foundation (NSF-0103082) for Nanotechnology Interdisciplinary Research Team (NIRT). Authors' special gratitude goes to Professor Katayun Barmak and Dr. Jihwan Kim from material science and engineering department of Carnegie Mellon University for the help with material characterization.

Appendix A

In the following, we have provided a relatively extensive background on the origin of Eq. (1). One can start with the governing energy equation for heat transfer in a fin of uniform cross-sectional area subjected to convective heat transfer with no heat generation [16],

$$\frac{d^2\Theta}{dx^2} - \frac{hP}{kA_c}\Theta = 0 \tag{A.1}$$

where P and A_c are the fin perimeter and cross-sectional area, respectively and $\Theta(x) = T(x) - T_\infty$. The thermal conductivity and convective heat transfer coefficient are k and h, respectively. For an infinite fin, the following two boundary conditions are defined: $T = T_b$ at $x = 0$ and $\Theta(L \to \infty) = 0$ at $x = L$. The temperature distribution in a long fin is given by

$$\Theta = \Theta_b e^{mx} \tag{A.2}$$

where

$$m = \sqrt{\frac{hP}{kA_c}} \tag{A.3}$$

The healing length, L_h, is defined as

$$L_h = \frac{1}{m} \tag{A.4}$$

which is a length of the fin over which the temperature is dropped by nearly 63% from the base temperature. L_h is the extent of lateral heat conduction in the fin and is a measure of the relative contribution of the heat conduction in the fin and the heat loss by convection heat transfer.

The concept of thermal healing length is often used in connection with heat conduction in a fin. However, it can also serve as a versatile tool in heat transfer analysis of the transistors, GMR and multi-layer thin film structures. Let us consider a thin film of high thermal conductivity material (e.g., silicon or GMR) and a low thermal conductivity underlayer (e.g., SiO_2, Al_2O_3) on a high thermal conductivity substrate such as silicon. Assume that the heat is generated by a deposited metal bridge on the top high thermal conductivity layer. The heat will be conducted both in the normal direction through the low thermal conductivity Al_2O_3 layer and laterally in the high thermal conductivity GMR layer. It can be shown that if certain conditions are satisfied [17] the temperature distribution in the high thermal conductivity layer can be approximated by Eq. (A.2). The heat transfer coefficient, h, should be now replaced by

$$h = \frac{k_{Gap}}{d_{Gap}} \tag{A.5}$$

By substituting the above equation into Eq. (A.4) and some algebraic manipulations, the extent of the lateral diffusion in the high thermal conductivity layer can be written as

$$L_h \sim \sqrt{\frac{d_{Gap} d_{GMR} k_{GMR}}{k_{Gap}}} \tag{A.6}$$

which is similar to Eq. (1).

The governing heat conduction equation for the self-heating in a GMR head is given by

$$\frac{d^2\Theta}{dx^2} + \frac{\dot{q}}{k} - m^2\Theta = 0 \tag{A.7}$$

While the temperature distribution given by the above equation is different from those given by Eq. (A.3), the physics of heat conduction in the GMR and Al_2O_3 structure remains the same. In this context, the healing length given by Eq. (A.6) can be used to define a modified cross-sectional area for thermal resistance across the gap layer given by Eq. (2).

References

[1] R.E. Fontana Jr., S.A. MacDonald, H.A.A. Santini, C. Tsang, Process considerations for critical features in high areal density thin film magnetoresistive heads: a review, IEEE Trans. Magnet. 35 (1999) 806–811.

[2] Y. Yang, S.M. Sadeghipour, M. Asheghi, Modeling of temperature rise in Giant Magnetoresistive (GMR) sensor during an Electrostatic Discharge (ESD) event, in: Proceeding of ASME Summer Heat Transfer Conference, HT2003-47266, 2003.

[3] C.A. Salama, RF sputtered aluminum oxide films on silicon, J. Electrochem. Soc. 117 (1970) 913–917.

[4] R.S. Nowicki, Origins and minimization of defects in sputtered thin films, Solid State Technol. 23 (1980) 83–88.

[5] R.A. Gardener, P.J. Peterson, T.N. Kennedy, Stability of RF-sputtered aluminum oxide, J. Vacuum Sci. Technol. 14 (1997) 1139–1145.

[6] Y. Kijima, T. Hanada, Effect of the pressure of sputtering atmosphere on the physical properties of amorphous aluminum oxide films, J. Mater. Sci. 35 (2000) 2193–2199.

[7] Y.S. Ju, R. Xu, X. Wu, N. Smith, R. Fontana, W. Lee, K. Carey, M. Ho, D. Hsiao, B. Gurney, A combined experimental and numerical study of temperature rise in GMR sensors due to self-heating, IEEE Trans. Magnet. 37 (2001) 1701–1703.

[8] C. Chang, Three-dimensional simulation of magnetoresistive heat temperature during ESD event, in: Proceedings of EOS/ESD Symposium, 1997, pp. 405–411.

[9] K. Young, Finite element analysis of planar stress anisotropy and thermal behavior in thin films, IBM J. Res. Develop. 34 (1990) 706–717.

[10] A. Wallash, T. Hughbanks, S. Voldman, ESD failure mechanisms of inductive and magentoresistive recoding heads, in: Proceedings of EOS/ESD Symposium, 1995, pp. 322–330.

[11] W.D. Greason, Electrostatic Discharge in Electronics, Wiley, New York, 1992, p. 150.

[12] MEMS Clearing House, 23 August 2002. Available from: <www.memsnet.org>.

[13] M. Asheghi, Y.K. Leung, S.S. Wong, K.E. Goodson, Phonon-boundary scattering in thin silicon layers, Appl. Phys. Lett. 71 (1997) 1798–1800.

[14] Y.S. Ju, K. Kurabayashi, K.E. Goodson, Thermal characterization of anisotropic thin dielectric films using harmonic Joule heating, Thin Solid Films (Elsevier) 339 (1999) 160–164.

[15] K.E. Goodson, Thermal conduction in microelectronic circuits, Ph.D. thesis, Massachusetts Institute of Technology, Cambridge, MA, 1993, pp. 112–116.
[16] F. Incropera, D. Dewitt, Introduction to Heat Transfer, third ed., Wiley, New York, 1966, pp. 110–120.
[17] M. Asheghi, M.N. Touzelbaev, K.E. Goodson, Y.K. Leung, S.S. Wong, Temperature dependent thermal conductivity of single-crystal silicon layers in SOI substrates, ASME J. Heat Transfer 120 (1998) 30–36.